

Mechanism of intermetallic charge transfer and bond disproportionation in BiNiO₃ and PbNiO₃ revealed by hard x-ray photoemission spectroscopy

Tatsuya Yamaguchi,¹ Mizuki Furo,¹ Yuki Sakai,^{2,3} Takumi Nishikubo,^{2,3} Hajime Hojo,⁴ Masaki Azuma,^{3,2} Kengo Oka,^{5,6} Daisuke Mori,^{7,8} Yoshiyuki Inaguma,⁷ Masaichiro Mizumaki,⁹ Kento Yamamoto,¹⁰ Jan Kuneš,^{11,12} Takashi Mizokawa,¹⁰ and Atsushi Hariki¹

¹*Department of Physics and Electronics, Graduate School of Engineering, Osaka Metropolitan University 1-1 Gakuen-cho, Nakaku, Sakai, Osaka 599-8531, Japan.*

²*Kanagawa Institute of Industrial Science and Technology (KISTEC), Ebina 243-0435, Japan*

³*Materials and Structures Laboratory, Institute of Innovative Research, Tokyo Institute of Technology 4259 Nagatsuta, Midori, Yokohama 226-8501, Japan*

⁴*Department of Advanced Materials Science and Engineering, Faculty of Engineering Sciences, Kyushu University, 6-1 Kasuga-koen, Kasuga, Fukuoka 816-8580, Japan*

⁵*Department of Applied Chemistry, Faculty of Science and Engineering, Chuo University, 1-13-27 Kasuga, Bunkyo-ku, Tokyo 112-8551, Japan.*

⁶*Department of Applied Chemistry, Faculty of Science and Engineering, Kindai University, 3-4-1 Kowakae, Higashi-Osaka, Osaka 577-8502, Japan.*

⁷*Department of Chemistry, Faculty of Science, Gakushuin University, 1-5-1 Mejiro, Toshima-ku, Tokyo 171-8588, Japan.*

⁸*Department of Applied Chemistry, Graduate School of Engineering, Mie University, Tsu, Mie 514-8507, Japan.*

⁹*Institute of Industrial Nanomaterials, Kumamoto University 2-39-1 Kurokami Chuo-ku Kumamoto 860-8555, Japan.*

¹⁰*Department of Applied Physics, Waseda University, 3-4-1 Okubo, Shinjuku-ku, Tokyo 169-8555, Japan.*

¹¹*Institute of Solid State Physics, TU Wien, 1040 Vienna, Austria*

¹²*Department of Condensed Matter Physics, Faculty of Science, Masaryk University, Kotlářská 2, 611 37 Brno, Czechia*

(Dated: May 15, 2024)

Perovskites with Bi or Pb on the A site host a number of interesting and yet to be understood phenomena such as negative thermal expansion in BiNiO₃. We employ hard x-ray photoemission spectroscopy of Ni 2*p* core level as well as valence band to probe the electronic structure of BiNiO₃ and PbNiO₃. The experimental results supported by theoretical calculations using dynamical mean-field theory reveal essentially identical electronic structure of the Ni–O subsystem typical of Ni²⁺ charge-transfer insulators. The two materials are distinguished by filling of the Bi(Pb)–O antibonding states in the vicinity of the Fermi level, which is responsible for the Bi disproportionation in BiNiO₃ at ambient pressure and absence of similar behavior in PbNiO₃. The present experiments provide evidence for this conclusion by revealing the presence/absence of Bi/Pb 6*s* states at the top of the valence band in the two materials.

I. INTRODUCTION

The A sites of typical AMO₃ perovskite transition-metal oxides (TMOs) are occupied by divalent alkaline earth metal or trivalent Y or rare-earth ions, which act as electron donors and form ionic bonds with oxygen. Perovskites with Pb or Bi on the A site are different. The Pb or Bi ions play a more active role thanks to their ability to form covalent bonds with oxygen. Both Pb and Bi belong to so-called valence skippers, ions that prefer to adopt the 6*s*⁰ (Pb⁴⁺, Bi⁵⁺) and 6*s*² (Pb²⁺, Bi³⁺) valence configurations while avoiding the 6*s*¹ (Pb³⁺, Bi⁴⁺) configuration. This behavior can be modelled with an attractive onsite interaction, negative *U*, within the 6*s* shell [1]. The origin of the negative *U* has been attributed to covalent bonding plus electron-lattice coupling [2] or nonlinear nonlocal screening [3].

Electronic structure calculations [4, 5] have shown that valence skipping in perovskite TMOs is caused by Pb(Bi)–O hybridization, which leads to formation of a

relatively narrow antibonding band. Its energy, determined by bonding-antibonding splitting, is sensitive to small changes of the Pb(Bi)–O bond lengths and therefore strongly coupled to the lattice [6]. Formal 6*s*⁰ and 6*s*² valence configurations correspond to a situation where the antibonding band is located above and below the Fermi level *E_F*, respectively. The 6*s*¹ or partially filled configurations would amount to pinning of the antibonding band at *E_F*. Such states/structures are often unstable towards small changes of the Pb(Bi)–O lengths, which cause the antibonding states to move away from *E_F*. This is accompanied by transfer of electrons/holes to other orbitals, e.g., TM 3*d* ones. Alternatively, Pb(Bi)–O bond-length disproportionation splits the antibonding band away from *E_F* and leads to redistribution of charge among inequivalent Pb(Bi) ions. While the negative *U* picture also leads to valence skipping it does not account for the geometrical constraints and correlations between Pb(Bi)–O bond lengths due to the A sites sharing their oxygen neighbors and vice versa. This affects possible

ordering patterns of $6s^2$ and $6s^0$ sites on the lattice [4, 5] as well as dynamics of the $6s$ electrons.

The Pb(Bi)–O hybridization picture can be probed by studying the Pb(Bi) $6s$ spectra. To this end, we have measured the valence and core-level x-ray photoemission spectroscopy (XPS) spectra of closely related PbNiO_3 and BiNiO_3 and analyzed them with the help of electronic structure calculations using local-density approximation (LDA) combined with dynamical mean-field theory (DMFT) method. We employ hard x-ray photoemission spectroscopy (HAXPES) which has large photoionization cross sections (CSs) for the Pb(Bi) $6s$ orbitals.

At ambient pressure BiNiO_3 is a good insulator [7] while PbNiO_3 shows a semiconducting behavior [8]. BiNiO_3 undergoes a pressure-driven metal-insulator transition (MIT) at the critical pressure 3.5 GPa [9, 10], which has been identified as a new type of MIT driven by electron transfer from Bi to Ni and interpreted using the negative U picture [11, 12]. At ambient pressure, BiNiO_3 is an insulator with two distinct Bi sites and formal valence $\text{Bi}_{0.5}^{3+}\text{Bi}_{0.5}^{5+}\text{Ni}^{2+}\text{O}_3$ [13]. At high pressure, it is a metal with formal valence $\text{Bi}^{3+}\text{Ni}^{3+}\text{O}_3$ [9, 10]. PbNiO_3 takes formal valence $\text{Pb}^{4+}\text{Ni}^{2+}\text{O}_3$.

II. METHODS

A. Experimental method

Polycrystalline samples of BiNiO_3 and PbNiO_3 were prepared under high pressure [8]. HAXPES measurements for valence band and Ni $2p$ core-level were performed at 300 K with photon energy of 7939.8 eV at the undulator beamlines BL47XU of SPring-8. For these measurements, hemispherical photoelectron analyzers (SES2002/R-4000) were used. The polycrystalline samples were fractured *in situ* for the XPS measurements. The binding energies were calibrated using Au $4f_{7/2}$ peak (84.0 eV) and Fermi edge of gold reference samples. The total energy resolution was 280 meV.

B. Computational method

The valence-band and core-level XPS spectra are simulated using the LDA+DMFT method [14–16]. The computation starts with a standard LDA calculation using Wien2k [17] for the experimental crystal structures of PbNiO_3 ($Pbn2_1$ space group) [18] and BiNiO_3 ($P\bar{1}$ space group) [13]. In BiNiO_3 , two inequivalent Bi sites [13] are present as shown in Fig. 1. The two Bi sites, with the shortest Bi–O bonds of 2.21 Å and 2.03 Å, are referred to as the “lone” and “pair” Bi ions hereafter.

Next, the LDA bands are mapped onto a tight-binding model spanning the Bi (Pb) $5d$, $6s$, $6p$, Ni $3d$, $4s$, O $2s$ and $2p$ bands [19, 20]. Although the low-energy electronic structures of the two compounds are governed by the Ni $3d$, O $2p$ and Bi (Pb) $6s$ states, the other orbitals can

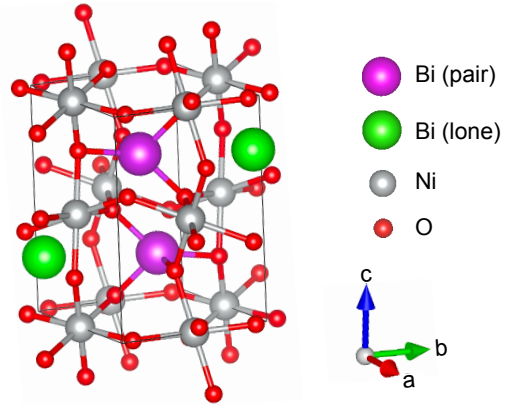


FIG. 1. Crystal structure of BiNiO_3 [13] visualized by VESTA [34].

be observed in the HAXPES spectra due to hybridization. The tight-binding model is augmented with a local electron-electron interaction within the Ni $3d$ shell. We employ Hubbard U and Hund’s J parameters of $(U, J) = (7.0 \text{ eV}, 1.1 \text{ eV})$ [21]. The double-counting correction μ_{dc} [16, 22] is set to reproduce the experimental valence-band and core-level spectra as in Refs. [23–25]. The details can be found in the Supplementary Material (SM) [26]. The strong-coupling continuous-time quantum Monte Carlo impurity solver [27–29] of the Anderson impurity model (AIM) is used to compute Ni $3d$ self-energies $\Sigma(i\omega_n)$. The valence-band spectra and hybridization densities $\Delta(\omega)$ on the real frequency axis are calculated from the local self-energy $\Sigma(\omega)$ analytically continued to the real-frequency axis using maximum entropy method [30, 31].

The Ni $2p$ core-level XPS spectra are calculated using a configuration-interaction impurity solver [23, 32, 33] from the DMFT AIM augmented with the Ni $2p$ core orbitals and their interaction with the valence electrons. The hybridization densities $\Delta(\omega)$ are represented by 25 discrete levels (per spin and orbital).

III. RESULTS AND DISCUSSION

A. Core-level XPS

We start our discussion with Ni $2p$ core-level XPS spectra. Figure 2 shows the Ni $2p$ XPS spectra of BiNiO_3 and PbNiO_3 measured at room temperature. Overall spectral shapes are similar to those of typical Ni^{2+} oxides, such as NiO [35] and La_2NiO_4 [36]. Both the $2p_{1/2}$ (884–868 eV) and $2p_{3/2}$ (868–852 eV) contributions consist of a main line (ML) and a satellite (ST). The Ni $2p_{3/2}$ ML in BiNiO_3 exhibits a shoulder on the higher-binding energy side, while the shoulder is less pronounced and the ML is more symmetric in PbNiO_3 . Given that the Néel temperatures of 300 K in BiNiO_3 and 225 K in PbNiO_3 [8, 13], we show the simulations for the an-

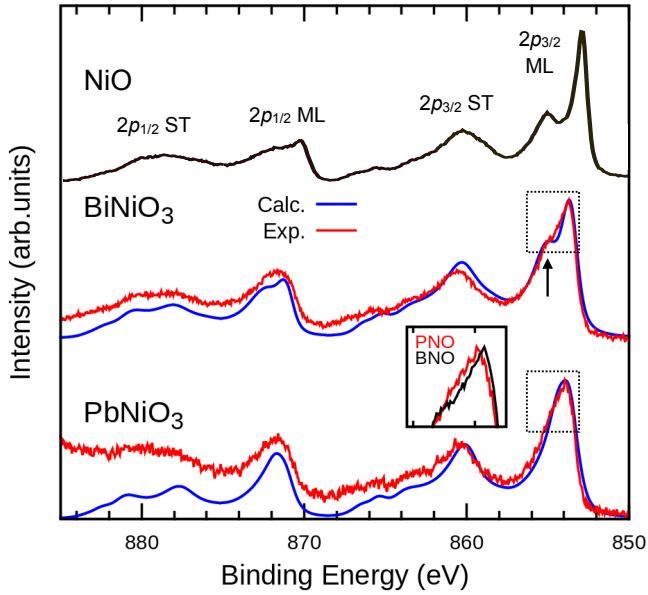


FIG. 2. The Ni $2p$ HAXPES experimental data (red) and the LDA+DMFT AIM calculations (blue) for BiNiO₃ in the AFI phase (middle) and PbNiO₃ (bottom) in the PMI phase. An arrow indicates the shoulder feature mentioned in the main text. The inset displays the magnified view of the Ni $2p_{3/2}$ ML in the experimental data for PbNiO₃ (PNO, red) and BiNiO₃ (BNO, black). The spectral broadening is considered using Gaussian of 300 meV and Lorentian of 300 meV (HWHM) in the calculated results. The Ni $2p$ XPS data of NiO [35] is shown for comparison (top). The Ni $2p_{3/2}$ ($2p_{1/2}$) main line (ML) and satellite (ST) are indicated.

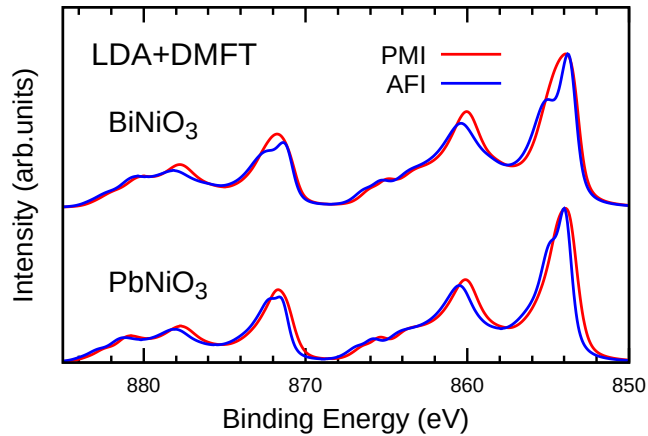


FIG. 3. The LDA+DMFT Ni $2p$ XPS spectra calculated for BiNiO₃ (top) and PbNiO₃ (bottom) in the paramagnetic insulating (red) and antiferromagnetic insulating (blue) phases.

tiferromagnetic insulating (AFI) phase for BiNiO₃ and the paramagnetic insulating (PMI) phase for PbNiO₃ in Fig. 2. Figure 3 shows that the spectra calculated within the same phase (i.e. AFI or PMI) are very similar in the two compounds, suggesting essentially identical electronic structures of Ni-O subsystems in BiNiO₃ and

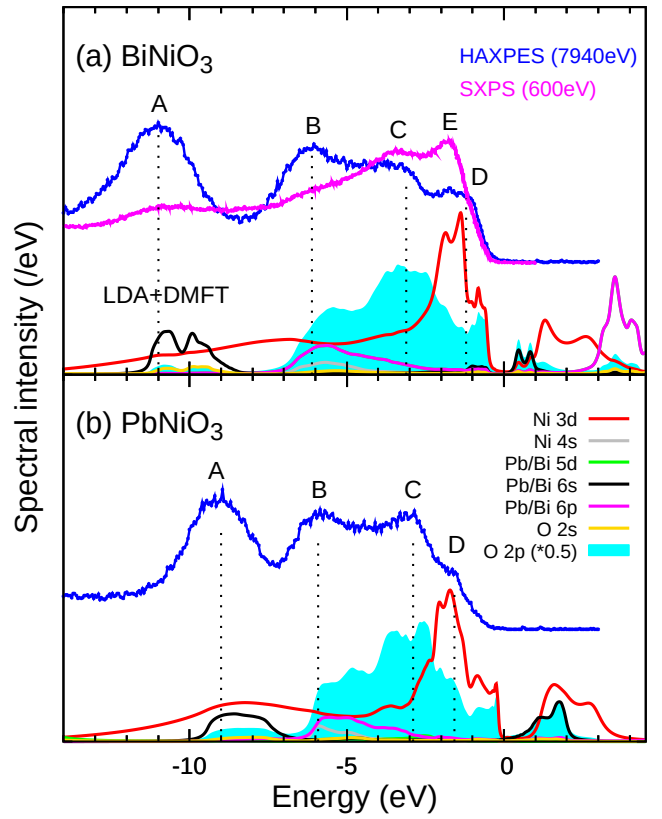


FIG. 4. The LDA+DMFT valence-band spectral intensities of (a) BiNiO₃ in the antiferromagnetic phase and (b) PbNiO₃ in the paramagnetic phase. The experimental valence-band spectra (blue) of BiNiO₃ [39, 40] and PbNiO₃ are shown for comparison.

PbNiO₃.

We briefly discuss the physical origin of the observed core-level spectra. Sudden creation of a localized core hole triggers a dynamical charge response in the XPS final states, which amounts to charge transfer (CT) from surrounding ligands as well as distant Ni ions to the excited Ni site, conventionally referred to as CT screening. The two components in the ML originate from two CT screening processes: one from nearest-neighboring ligands and the other, at lower binding energy, from distant Ni ions, often called local and nonlocal screening, respectively [35, 37, 38]. The nonlocal CT screening in Ni²⁺ oxides [23, 38] is less efficient in PMI than in AFI due to Pauli blocking, which explains the suppression of low-energy peak in PMI.

B. Valence-band XPS

Figure 4 shows the experimental and LDA+DMFT valence-band spectra of BiNiO₃ [40] and PbNiO₃. Soft x-ray XPS (SXPS) spectrum of Bi_{0.95}La_{0.05}NiO₃ measured at photon energy of 600 eV [39] is shown for comparison. The difference between the spectra obtained with hard

	8000 eV			500 eV	
	β	σ [b]	$d\sigma/d\Omega$ [b/sr]	σ [b]	$d\sigma/d\Omega$ [b/sr]
Ni 3d	0.322	0.741	0.078	19.969	1.589
Ni 4s	1.960	6.855	1.615	2.569	0.204
Bi 5d	1.198	68.690	12.014	14.282	1.137
Bi 6s	1.890	25.050	5.761	2.658	0.212
Bi 6p	1.731	14.340	3.116	1.569	0.125
Pb 5d	1.184	59.350	10.317	13.116	1.044
Pb 6s	1.898	21.495	4.957	2.338	0.186
Pb 6p	1.653	13.475	2.845	0.983	0.078
O 2s	1.923	6.795	1.581	11.510	0.916
O 2p	0.053	0.080	0.007	2.214	0.176

TABLE I. Subshell photoionization cross section σ at 8000 eV (hard X-ray) and 500 eV (soft X-ray) for relevant orbitals [42–44]. The differential cross section $d\sigma/d\Omega$ at 8000 eV is calculated taking the dipole parameter β for the angular distribution into account. To simulate the experimental geometry in the previous SXPS study in Ref. [39], β is not considered for $d\sigma/d\Omega$ at 500 eV.

and soft x rays reflects the different photon-energy dependencies of the photoionization CSs for the constituent orbitals. The empirical CS values summarized in Table I show that while Ni 3d orbitals have large CS at 500 eV, at 7940 eV the Bi (Pb) CSs are dominant. This makes the hard x rays well suited to study the Bi and Pb 6s states.

We identify features labeled as *A*, *B*, *C*, *D* in the HAXPES spectra of BiNiO₃ and PbNiO₃. In addition, a feature *E*, enhanced in soft x-ray spectra, is attributed to the Ni 3d orbital contributions and matches well the position of the Ni 3d peak in the LDA+DMFT result. The peak *A* corresponds to Bi (Pb) 6s states—bonding state in the language of Bi(Pb)–O hybridization. On the other hand, peak *D* gains its weight in the HAXPES spectrum of BiNiO₃, peak *D* of BiNiO₃ can be assigned to Bi 6s or 6p.

In order to identify the origin of features *B*, *C*, *D*, we weight the LDA+DMFT valence-band intensities with the CSs at 7940 eV in Fig. 5. An underestimate (~ 0.5 eV) of the binding energies of the feature *A* is due to uncertainty in the adopted approximation for the exchange-correlation potential [41]. Although the Bi (Pb) 5d and 6p states are positioned far below and above E_F , see SM [26], their CSs are extremely large in the hard x-ray regime, Table I. This together with a tiny hybridization with the valence band makes them apparent in the HAXPES spectra in the valence region. The simulated spectra in Fig. 5 show that the Bi or Pb 6p states are important for the feature *B*, while the 5d states give rise to the feature *C*. The shallower Pb 5d states could explain the enhanced intensity of the feature *C* in PbNiO₃ compared to that in BiNiO₃.

The main qualitative difference between the HAXPES spectra of BiNiO₃ and PbNiO₃ is the enhanced spectral

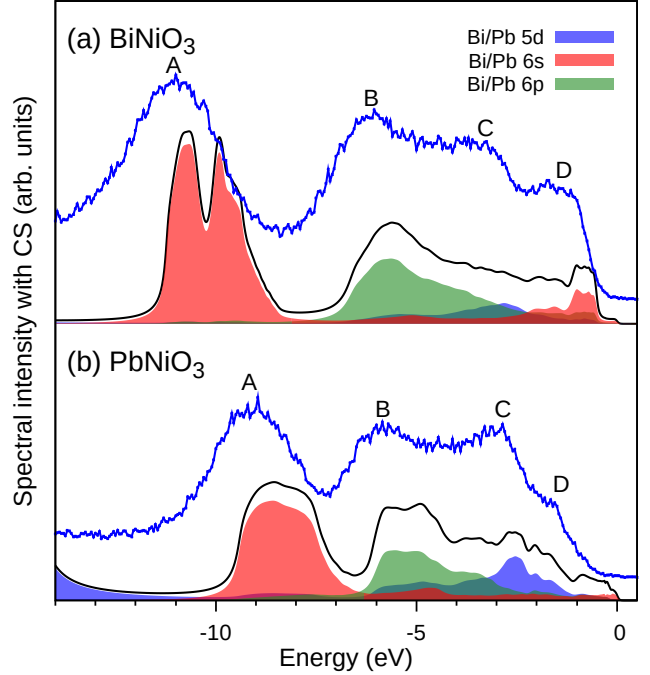


FIG. 5. The LDA+DMFT valence-band spectral intensities of (a) BiNiO₃ in the antiferromagnetic phase and (b) PbNiO₃ in the paramagnetic phase weighted with the CSs listed in Table I. The Fermi-Dirac function at 300 K is included in the theoretical spectra. The filled curves show the contributions of the Bi (Pb) 5d, 6s and 6p states. The experimental HAXPES data (blue) of BiNiO₃ [40] and PbNiO₃ are shown for comparison.

weight at the top of the valence band. The analysis of Fig. 5 links it to the presence of Bi 6s orbital character, while Pb 6s states are missing at the valence-band top in PbNiO₃. To isolate the physics of Bi(Pb) 6s–O 2p bonding, we present, in Fig. 6, the Bi(Pb) 6s and O 2p spectral densities obtained with the Ni–O and Ni–Bi(Pb) hopping artificially switched off in the LDA+DMFT valence-band models in Fig. 4. Besides the quantitative differences consisting in shallower 6s states for lighter Pb and the resulting somewhat stronger covalent character of the Pb–O bond, there is a qualitative difference reflecting the disproportionation of the Bi sites. This leads to splitting of the antibonding band into states associated with the lone Bi site at lower and pair Bi sites at higher energies, consistent with the previous GGA+*U* and DMFT studies [4, 45]. No splitting of the antibonding band takes place in PbNiO₃. This picture, necessarily with broader and richer structures in the 6s spectra, is preserved when Ni is fully included. The CT gap of Ni–O subsystem overlaps with lone-pair antibonding gap in BiNiO₃ and O 2p-antibonding gap in PbNiO₃ in Fig. 4.

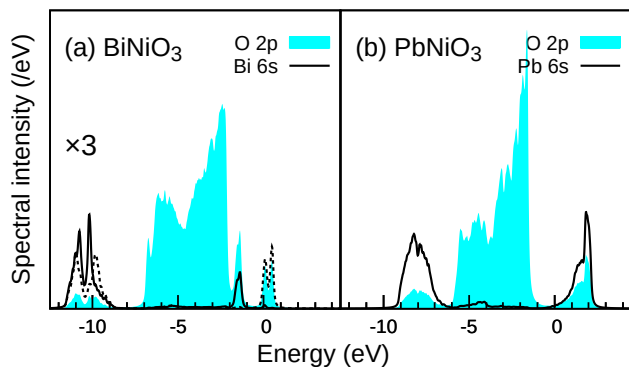


FIG. 6. The valence-band spectra in (a) BiNiO_3 and (b) PbNiO_3 sublattice computed by removing the Ni $3d$ orbitals in the LDA+DMFT valence-band models in Figs. 4ab. The Bi and Pb $6s$ spectral weights are magnified by the factor of 3. The solid (dashed) line in BiNiO_3 represents lone (pair) Bi site contribution.

IV. CONCLUSIONS

We have presented a comparative study of two A-site active nickelates BiNiO_3 and PbNiO_3 . The valence and Ni $2p$ core-level photoemission experiments supported by LDA+DMFT calculations reveal essentially identical electronic structures of Ni–O subsystems in the two compounds, characteristic of Ni^{2+} in charge-transfer systems such as NiO [46–48]. The main difference between the two compounds is derived from the Pb(Bi) $6s$ orbitals. The calculations find strong Pb(Bi)–O hybridization leading to bonding-antibonding splitting of almost 10 eV, with the antibonding states located within the charge-transfer gap. In PbNiO_3 , electron counting places the Fermi level below the antibonding band, while in BiNiO_3 the Fermi level falls in the middle of the antibonding band. This situation in the latter is resolved by disproportionation of the Bi–O bonds, which gives rise to two distinct Bi sites, with antibonding states above and below the Fermi level.

Our main experimental result is the observation of the Bi–O antibonding states at the top of the valence band, which confirms the above mechanism of Bi disproportionation. We conclude our presentation by commenting on the relationship of the present description to the negative U model of valence skippers. The negative U model qualitatively explains presence (absence) of A-site disproportionation in BiNiO_3 (PbNiO_3). It can be viewed as an effective model for the Pb(Bi)–O antibonding states obtained by the process of integrating out the O states. However, in this process also nonlocal interaction terms are expected to appear, e.g., due to O site having several Pb(Bi) neighbors. Such terms determine the pattern of disproportionated Bi ions on the lattice.

A question also arises about the negative U treatment of possible superconductivity in materials with valence skippers. Strong covalent bonds in systems with antibonding states at the Fermi level result in a strong electron-phonon coupling [6]. As in other such materials, superconductivity is competing with a structural instability. The capability of the negative U model to capture this competition appears questionable and we find that the full treatment of Pb(Bi)–O bonding without the effective $6s$ interaction U preferable.

ACKNOWLEDGMENTS

This work was supported by JSPS KAKENHI Grants No. 21K13884, No. 21H01003, No. 23K03324, No. 23H03816, No. 23H03817 (A.H.), JP19H0562 and JSTCREST (JPMJCR2201) (M.A.), and by the Project No. CZ.02.01.01/00/22_008/0004572 of the Programme Johannes Amos Comenius (J.K.). The synchrotron-radiation experiments were performed at SPring-8 with the approval of the Japan Synchrotron Radiation Research Institute (2017B1721). The authors would like to thank Dr. Shigenori Ueda for the contribution to HAX-PES measurements at BL15XU, SPring8, in the early stage of this work.

-
- [1] H. Matsuura, H. Mukuda, and K. Miyake, Valence skipping phenomena, charge kondo effect, and superconductivity, *AAPS Bulletin* **32**, 30 (2022).
 - [2] P. W. Anderson, Model for the Electronic Structure of Amorphous Semiconductors, *Phys. Rev. Lett.* **34**, 953 (1975).
 - [3] C. M. Varma, Missing valence states, diamagnetic insulators, and superconductors, *Phys. Rev. Lett.* **61**, 2713 (1988).
 - [4] A. Paul, A. Mukherjee, I. Dasgupta, A. Paramekanti, and T. Saha-Dasgupta, Hybridization-switching induced mott transition in $ab\text{O}_3$ perovskites, *Phys. Rev. Lett.* **122**, 016404 (2019).
 - [5] A. Hariki, K.-H. Ahn, and J. Kuneš, Valence skipping, internal doping, and site-selective Mott transition in PbCoO_3 under pressure, *Phys. Rev. B* **104**, 235101 (2021).
 - [6] J. M. An and W. E. Pickett, Superconductivity of MgB_2 : Covalent Bonds Driven Metallic, *Phys. Rev. Lett.* **86**, 4366 (2001).
 - [7] S. Ishiwata, M. Azuma, M. Hanawa, Y. Moritomo, Y. Ohishi, K. Kato, M. Takata, E. Nishibori, M. Sakata, I. Terasaki, and M. Takano, Pressure/temperature/substitution-induced melting of A-site charge disproportionation in $\text{Bi}_{1-x}\text{La}_x\text{NiO}_3$ ($0 \leq x \leq 0.5$), *Phys. Rev. B* **72**, 045104 (2005).
 - [8] Y. Inaguma, K. Tanaka, T. Tsuchiya, D. Mori, T. Katsumata, T. Ohba, K.-i. Hiraki, T. Takahashi, and H. Saitoh, Synthesis, Structural Transformation, Thermal Stability, Valence State, and Magnetic and Elec-

- tronic Properties of PbNiO_3 with Perovskite- and LiNbO_3 -Type Structures, *J. Am. Chem. Soc.* **133**, 16920 (2011).
- [9] M. Azuma, W.-t. Chen, H. Seki, M. Czapski, S. Olga, K. Oka, M. Mizumaki, T. Watanuki, N. Ishimatsu, N. Kawamura, S. Ishiwata, M. G. Tucker, Y. Shimakawa, and J. P. Attfield, Colossal negative thermal expansion in BiNiO_3 induced by intermetallic charge transfer, *Nat. Commun.* **2**, 347 (2011).
- [10] M. Azuma, S. Carlsson, J. Rodgers, M. G. Tucker, M. Tsujimoto, S. Ishiwata, S. Isoda, Y. Shimakawa, M. Takano, and J. P. Attfield, Pressure-Induced Intermetallic Vence Transition in BiNiO_3 , *J. Am. Chem. Soc.* **129**, 14433 (2007).
- [11] M. Naka, H. Seo, and Y. Motome, Theory of Valence Transition in BiNiO_3 , *Phys. Rev. Lett.* **116**, 056402 (2016).
- [12] S. Kojima, J. Nasu, and A. Koga, Phase transitions in the Hubbard model for the bismuth nickelate, *Phys. Rev. B* **94**, 045103 (2016).
- [13] S. Ishiwata, M. Azuma, M. Takano, E. Nishibori, M. Takata, M. Sakata, and K. Kato, High pressure synthesis, crystal structure and physical properties of a new Ni(ii) perovskite BiNiO_3 , *J. Mater. Chem.* **12**, 3733 (2002).
- [14] W. Metzner and D. Vollhardt, Correlated Lattice Fermions in $d = \infty$ Dimensions, *Phys. Rev. Lett.* **62**, 324 (1989).
- [15] A. Georges, G. Kotliar, W. Krauth, and M. J. Rozenberg, Dynamical mean-field theory of strongly correlated fermion systems and the limit of infinite dimensions, *Rev. Mod. Phys.* **68**, 13 (1996).
- [16] G. Kotliar, S. Y. Savrasov, K. Haule, V. S. Oudovenko, O. Parcollet, and C. A. Marianetti, Electronic structure calculations with dynamical mean-field theory, *Rev. Mod. Phys.* **78**, 865 (2006).
- [17] P. Blaha, K. Schwarz, G. Madsen, D. Kvasnicka, and J. Luitz, *WIEN2k, An Augmented Plane Wave + Local Orbitals Program for Calculating Crystal Properties* (Karlheinz Schwarz, Techn. Universitat Wien, Austria, 2001, ISBN 3-9501031-1-2, 2018).
- [18] Y. Sakai, T. Nishikubo, T. Ogata, H. Ishizaki, T. Imai, M. Mizumaki, T. Mizokawa, A. Machida, T. Watanuki, K. Yokoyama, Y. Okimoto, S.-y. Koshihara, H. Das, and M. Azuma, Polar-Nonpolar Phase Transition Accompanied by Negative Thermal Expansion in Perovskite-Type $\text{Bi}_{1-x}\text{Pb}_x\text{NiO}_3$, *Chem. Mater.* **31**, 4748 (2019).
- [19] J. Kuneš, R. Arita, P. Wissgott, A. Toschi, H. Ikeda, and K. Held, Wien2wannier: From linearized augmented plane waves to maximally localized Wannier functions, *Comput. Phys. Commun.* **181**, 1888 (2010).
- [20] A. A. Mostofi, J. R. Yates, G. Pizzi, Y.-S. Lee, I. Souza, D. Vanderbilt, and N. Marzari, An updated version of wannier90: A tool for obtaining maximally-localised Wannier functions, *Comput. Phys. Commun.* **185**, 2309 (2014).
- [21] V. I. Anisimov, J. Zaanen, and O. K. Andersen, Band theory and Mott insulators: Hubbard u instead of Stoner i , *Phys. Rev. B* **44**, 943 (1991).
- [22] M. Karolak, G. Ulm, T. Wehling, V. Mazurenko, A. Poteryaev, and A. Lichtenstein, Double counting in LDA + DMFT - The example of NiO, *J. Electron Spectrosc. Relat. Phenom.* **181**, 11 (2010).
- [23] A. Hariki, T. Uozumi, and J. Kuneš, LDA+DMFT approach to core-level spectroscopy: Application to $3d$ transition metal compounds, *Phys. Rev. B* **96**, 045111 (2017).
- [24] K. Higashi, M. Winder, J. Kuneš, and A. Hariki, Core-Level X-Ray Spectroscopy of Infinite-Layer Nickelate: LDA + DMFT Study, *Phys. Rev. X* **11**, 041009 (2021).
- [25] A. Hariki, K. Higashi, T. Yamaguchi, J. Li, C. Kalha, M. Mascheck, S. K. Eriksson, T. Wiell, F. M. F. de Groot, and A. Regoutz, Satellites in the Ti $1s$ core level spectra of SrTiO_3 and TiO_2 , *Phys. Rev. B* **106**, 205138 (2022).
- [26] See Supplementary Material for details at ...
- [27] P. Werner, A. Comanac, L. de' Medici, M. Troyer, and A. J. Millis, Continuous-Time Solver for Quantum Impurity Models, *Phys. Rev. Lett.* **97**, 076405 (2006).
- [28] L. Boehnke, H. Hafermann, M. Ferrero, F. Lechermann, and O. Parcollet, Orthogonal polynomial representation of imaginary-time Green's functions, *Phys. Rev. B* **84**, 075145 (2011).
- [29] H. Hafermann, K. R. Patton, and P. Werner, Improved estimators for the self-energy and vertex function in hybridization-expansion continuous-time quantum Monte Carlo simulations, *Phys. Rev. B* **85**, 205106 (2012).
- [30] X. Wang, E. Gull, L. de' Medici, M. Capone, and A. J. Millis, Antiferromagnetism and the gap of a Mott insulator: Results from analytic continuation of the self-energy, *Phys. Rev. B* **80**, 045101 (2009).
- [31] M. Jarrell and J. Gubernatis, Bayesian inference and the analytic continuation of imaginary-time quantum Monte Carlo data, *Phys. Rep.* **269**, 133 (1996).
- [32] M. Ghiasi, A. Hariki, M. Winder, J. Kuneš, A. Regoutz, T.-L. Lee, Y. Hu, J.-P. Rueff, and F. M. F. de Groot, Charge-transfer effect in hard x-ray $1s$ and $2p$ photoemission spectra: LDA + DMFT and cluster-model analysis, *Phys. Rev. B* **100**, 075146 (2019).
- [33] M. Winder, A. Hariki, and J. Kuneš, X-ray spectroscopy of the rare-earth nickelate LuNiO_3 : LDA + DMFT study, *Phys. Rev. B* **102**, 085155 (2020).
- [34] K. Momma and F. Izumi, *VESTA3* for three-dimensional visualization of crystal, volumetric and morphology data, *J. Appl. Crystall.* **44**, 1272 (2011).
- [35] M. Taguchi, M. Matsunami, Y. Ishida, R. Eguchi, A. Chainani, Y. Takata, M. Yabashi, K. Tamasaku, Y. Nishino, T. Ishikawa, Y. Senba, H. Ohashi, and S. Shin, Revisiting the Valence-Band and Core-Level Photoemission Spectra of NiO, *Phys. Rev. Lett.* **100**, 206401 (2008).
- [36] H. Eisaki, S. Uchida, T. Mizokawa, H. Namatame, A. Fujimori, J. van Elp, P. Kuiper, G. A. Sawatzky, S. Hosoya, and H. Katayama-Yoshida, Electronic structure of $\text{La}_{2-x}\text{Sr}_x\text{NiO}_4$ studied by photoemission and inverse-photoemission spectroscopy, *Phys. Rev. B* **45**, 12513 (1992).
- [37] M. A. van Veenendaal and G. A. Sawatzky, Nonlocal screening effects in $2p$ x-ray photoemission spectroscopy core-level line shapes of transition metal compounds, *Phys. Rev. Lett.* **70**, 2459 (1993).
- [38] A. Hariki, Y. Ichinozuka, and T. Uozumi, Dynamical Mean-Field Approach to Ni $2p$ X-ray Photoemission Spectra of NiO: A Role of Antiferromagnetic Ordering, *J. Phys. Soc. Jpn.* **82**, 043710 (2013).
- [39] H. Wadati, K. Tanaka, A. Fujimori, T. Mizokawa, H. Kumigashira, M. Oshima, S. Ishiwata, M. Azuma, and M. Takano, Temperature-dependent photoemission and x-ray absorption studies of the metal-insulator transition

- in $\text{Bi}_{1-x}\text{La}_x\text{NiO}_3$, *Phys. Rev. B* **76**, 205123 (2007).
- [40] T. Nishikubo, Y. Sakai, K. Oka, T. Watanuki, A. Machida, M. Mizumaki, K. Maebayashi, T. Imai, T. Ogata, K. Yokoyama, Y. Okimoto, S. Koshihara, H. Hojo, T. Mizokawa, and M. Azuma, Enhanced Negative Thermal Expansion Induced by Simultaneous Charge Transfer and Polar–Nonpolar Transitions, *J. Am. Chem. Soc.* **141**, 19397 (2019).
- [41] X. F. Hao, A. Stroppa, P. Barone, A. Filippetti, C. Franchini, and S. Picozzi, Structural and ferroelectric transitions in magnetic nickelate PbNiO_3 , *New J. Phys.* **16**, 015030 (2014).
- [42] M. Trzhaskovskaya and V. Yarzhemsky, Dirac–Fock photoionization parameters for HAXPES applications, *At. Data Nucl. Data Tables* **119**, 99 (2018).
- [43] M. Trzhaskovskaya, V. Nefedov, and V. Yarzhemsky, PHOTOELECTRON ANGULAR DISTRIBUTION PARAMETERS FOR ELEMENTS $Z=1$ TO $Z=54$ IN THE PHOTOELECTRON ENERGY RANGE 100–5000 eV, *At. Data Nucl. Data Tables* **77**, 97 (2001).
- [44] M. Trzhaskovskaya, V. Nefedov, and V. Yarzhemsky, PHOTOELECTRON ANGULAR DISTRIBUTION PARAMETERS FOR ELEMENTS $Z=55$ TO $Z=100$ IN THE PHOTOELECTRON ENERGY RANGE 100–5000 eV, *At. Data Nucl. Data Tables* **82**, 257 (2002).
- [45] I. Leonov, A. S. Belozarov, and S. L. Skornyakov, Unusual mott transition associated with charge-order melting in binio_3 under pressure, *Phys. Rev. B* **100**, 161112 (2019).
- [46] G. A. Sawatzky and J. W. Allen, Magnitude and origin of the band gap in nio , *Phys. Rev. Lett.* **53**, 2339 (1984).
- [47] A. Fujimori, F. Minami, and S. Sugano, Multielectron satellites and spin polarization in photoemission from Ni compounds, *Phys. Rev. B* **29**, 5225 (1984).
- [48] J. Kuneš, V. I. Anisimov, A. V. Lukoyanov, and D. Vollhardt, Local correlations and hole doping in nio : A dynamical mean-field study, *Phys. Rev. B* **75**, 165115 (2007).